
Reinforcement Learning for Chemical Ordering in Alloy Nanoparticles

Jonas Elsborg^{1,2} Arghya Bhowmik^{1,2*}

¹Department of Energy Conversion and Storage, Technical University of Denmark

²CAPEX Pioneer Center for Accelerating P2X Materials Discovery

Abstract

We approach the search for optimal element ordering in bimetallic alloy nanoparticles (NPs) as a reinforcement learning (RL) problem, and have built an RL agent that learns to perform such global optimisation using the geometric graph representation of the NPs. To demonstrate the effectiveness, we train an RL agent to perform composition-conserving atomic swap actions on the icosahedral nanoparticle structure. Trained once on randomised $\text{Ag}_x\text{Au}_{309-x}$ compositions and orderings, the agent discovers previously established ground state structure. We show that this optimization is robust to differently ordered initialisations of the same NP compositions. We also demonstrate that a trained policy can extrapolate effectively to NPs of unseen size. However, the efficacy is limited when multiple alloying elements are involved. Our results demonstrate that RL with pre-trained equivariant graph encodings can navigate combinatorial ordering spaces at the nanoparticle scale, and offer a transferable optimisation strategy with the potential to generalise across composition and reduce repeated individual search cost.

1 Introduction

Metallic nanoparticles (NPs) are widely used as heterogeneous (electro)catalysts because their high site-to-volume ratios and tunable active sites enable exceptional reactivity (Narayan et al., 2019; McIntyre & Garden, 2025). The elemental composition, size, shape, and atomic ordering of NPs directly influence their catalytic properties and stability by determining the distribution and nature of active sites on the surface (Loevlie et al., 2023). Determining the atomic structure of NPs is therefore a central objective in designing efficient and selective catalysts, and several computational strategies have been developed to resolve their ground-state atomic arrangements Loevlie et al. (2023). However, NP structure search faces two central challenges: the high cost of evaluating the total energy of a given atomic structure/ordering to assess its stability, and the limited efficiency of algorithms for exploring the structure/ordering space using this energy evaluator. As a result, most NP structure searches rely on inexpensive classical potentials (Lysgaard et al., 2014; Zhang et al., 2015; Cerbelaud et al., 2011), while first-principles Density Functional Theory (DFT) is generally too computationally expensive to use in the search itself and is instead reserved for validating a limited set of candidate structures Zhang et al. (2015); Negreiros et al. (2010). Recently, machine learning (ML) potentials have been used to accelerate the energy evaluation step while retaining near-DFT accuracy in energetics Han et al. (2022); Álvarez-Zapatero et al. (2021); Ojha et al. (2024). The search space for possible atomic configurations grows combinatorially with cluster size, and constructing effective search algorithms is equally crucial and can be paired with all different energy evaluation methods. Mixed-integer programming (MIP) Larsen et al. (2018), Monte Carlo (MC) sampling Artrith & Kolpak (2015); Pirart et al. (2019); Bochicchio et al. (2014), and basin hopping (BH) Gould et al. (2014); Cheng et al. (2013); Rondina & Da Silva (2013); Bochicchio & Ferrando

*Corresponding author: arbh@dtu.dk

(2013) techniques have been used to determine provably optimal structures (within the accuracy of the energy/fitness function). Genetic algorithms (GAs) explore the vast combinatorial configuration space by iteratively evolving a population of candidate structures, and are generally more efficient and popular (Chen & Johnston, 2008; Froemming & Henkelman, 2009; Loevlie et al., 2023; Lysgaard et al., 2014, 2015; Han et al., 2022; Rodrigues et al., 2008; Zhang et al., 2015; Tao et al., 2017; Dean et al., 2020; Liu et al., 2016; Rapallo et al., 2005). For each GA run, one must evaluate the fitness (energy) of many candidates over numerous generations. However, GA and other classical methods like MC are intractable for larger systems, and a significant drawback from these methods is the non-transferability and lack of generalisation across different compositions, forcing independent optimisation runs for each elemental composition or NP size separately.

Recent work has turned to reinforcement learning (RL) as a unified optimisation approach for atomic structures (Ahmed et al., 2025). An RL agent can be trained to construct molecules or nanoparticle structures atom-by-atom (Simm et al., 2020; Elsborg & Bhowmik, 2023), or even fragment-by-fragment (Flam-Shepherd et al., 2022). Another approach is to train RL agents to modify an existing structure by treating the configuration space as a labelled graph, which the RL agent learns to reconfigure (Elsborg & Bhowmik, 2024). The benefit of a trained RL policy is that it can rapidly propose near-optimal configurations without performing an exhaustive search from scratch for each structure or composition. So far, this approach has been explored only for nanoparticles with small number of atoms (Elsborg & Bhowmik, 2023; Ahmed et al., 2025). In this work, we built and deployed a reinforcement learning framework that couples an equivariant encoder (Rhodes et al., 2025) with a reinforcement learning model trained via proximal policy optimisation (PPO) to perform composition-preserving structure manipulation actions on the atomic graph to optimise ordering. Trained once, the agent reproduces a set of provably exact ground state orderings of Mackay-icosahedral $\text{Ag}_x\text{Au}_{309-x}$ nanoparticles.

2 Methods

2.1 Nanoparticle optimisation as a reinforcement learning problem

We formulate the search for a minimum-energy nanoparticle structure as a sequential decision-making task, i.e., a Markov Decision Process (MDP). In this MDP, a state s_t represents an atomic configuration of a NP (positions and types of all atoms) at time step t in the MDP. In our setting, an action a_t at time t corresponds to a modification of the NP structure resulting from swapping the positions $\mathbf{x}_A = (x_A, y_A, z_A)$ and $\mathbf{x}_B = (x_B, y_B, z_B)$ of two atoms A and B. The environment computes the potential energy of the resulting structure and returns a reward $r_t = E(s_t) - E(s_{t+1})$ based on the energy change between the energy of the pre-swap state, $E(s_t)$, and that of the post-swap state, $E(s_{t+1})$. After each action, we also perform a local geometry relaxation.

Thus, if $r_t > 0$, the atomic swap resulted in a lower-energy state at $t + 1$ than at t . This approach incentivises the agent to move toward more stable configurations. It also fully satisfies the Markov property (the energy outcome depends only on the current atomic arrangement) and provides a dense scalar reward. Maximising the return G , i.e. the cumulative reward, over a horizon of H actions corresponds to minimising the NP’s energy. This results in a sum that signals the overall energy difference between the initial state and the final state (assuming no discount factor is used, see Appendix A.1). The formulation allows the agent to explore the configurational space in a guided manner since it learns a policy that, at each step, chooses how to alter the NP to reach a lower-energy state at the end. By maximising G , the agent can discover non-trivial sequences of modifications that yield large net energy drops, even if some intermediate steps may lead to an increase in energy. This ability of RL to handle long-term credit assignment (assigning credit to actions that lead to benefits much later) is a key advantage in navigating complex energy landscapes with many local minima.

Recent studies have demonstrated that policy-based RL agents can efficiently navigate such energy landscapes to find stable, low-energy structures of molecules, metal clusters and bulk materials (Simm et al., 2020; Flam-Shepherd et al., 2022; Elsborg & Bhowmik, 2023, 2024). To evaluate the energy of NPs, we use the Effective Medium Theory (EMT) potential - a semi-empirical many-body potential (Jacobsen et al., 1996). Even though EMT has relatively cheap energy evaluations, the search for global minima can be very expensive as the number of chemical orderings grows combinatorially. For a fixed shape with N sites and bimetallic composition A_xB_{N-x} , the labellings scale as $\binom{N}{x}$. For example, in a 309-atom icosahedral NP ($\text{Ag}_x\text{Au}_{309-x}$) with elemental composition of $\text{Ag}_{162}\text{Au}_{147}$, we

get $\binom{309}{162} \approx 3.3 \times 10^{91}$ chemical orderings, and symmetry reduces this only by a modest constant factor (Dean et al., 2020).

2.2 RL Algorithm: Actor–Critic with PPO and KL Regularisation

We adopt an actor–critic version of the proximal policy optimisation algorithm (Schulman et al., 2017) (PPO) to train the agent’s policy. The actor is the policy $\pi_{\theta}(a | s)$, parametrised by weights θ , used to predict a distribution over actions a_t given state s_t at time t . The critic is a value function $V_{\phi}(s_t)$, with parameters ϕ , and estimates the expected cumulative reward (proportional to the expected energy reduction) from s_t . By teaching the critic to predict the state values, the actor can learn to select actions that yield high returns as judged by the critic’s feedback. We use generalised advantage estimation (Schulman et al., 2015b) (GAE) to compute the advantage of an action a_t compared to default behaviour (expectation under the value function). All algorithm details are in Appendix A. Due to our definition of MDP as a sequence of atomic swap actions, we define a single atom swap action as the choice of an atom pair $a_t = (i_t, j_t)$. Thus, at each time step t , the agent picks an *anchor* atom i which is then paired with a suitable *partner* atom indexed by j (Figure 1).

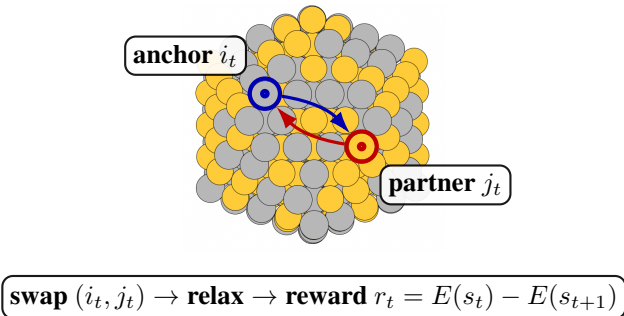


Figure 1: Agent–environment step on the Ag/Au NP: highlight the chosen **anchor** i and **partner** j , swap species, relax, compute reward, and continue. In Figure 7 in Appendix C, we show snapshots from a full episode of anchor-partner swaps for a trained model.

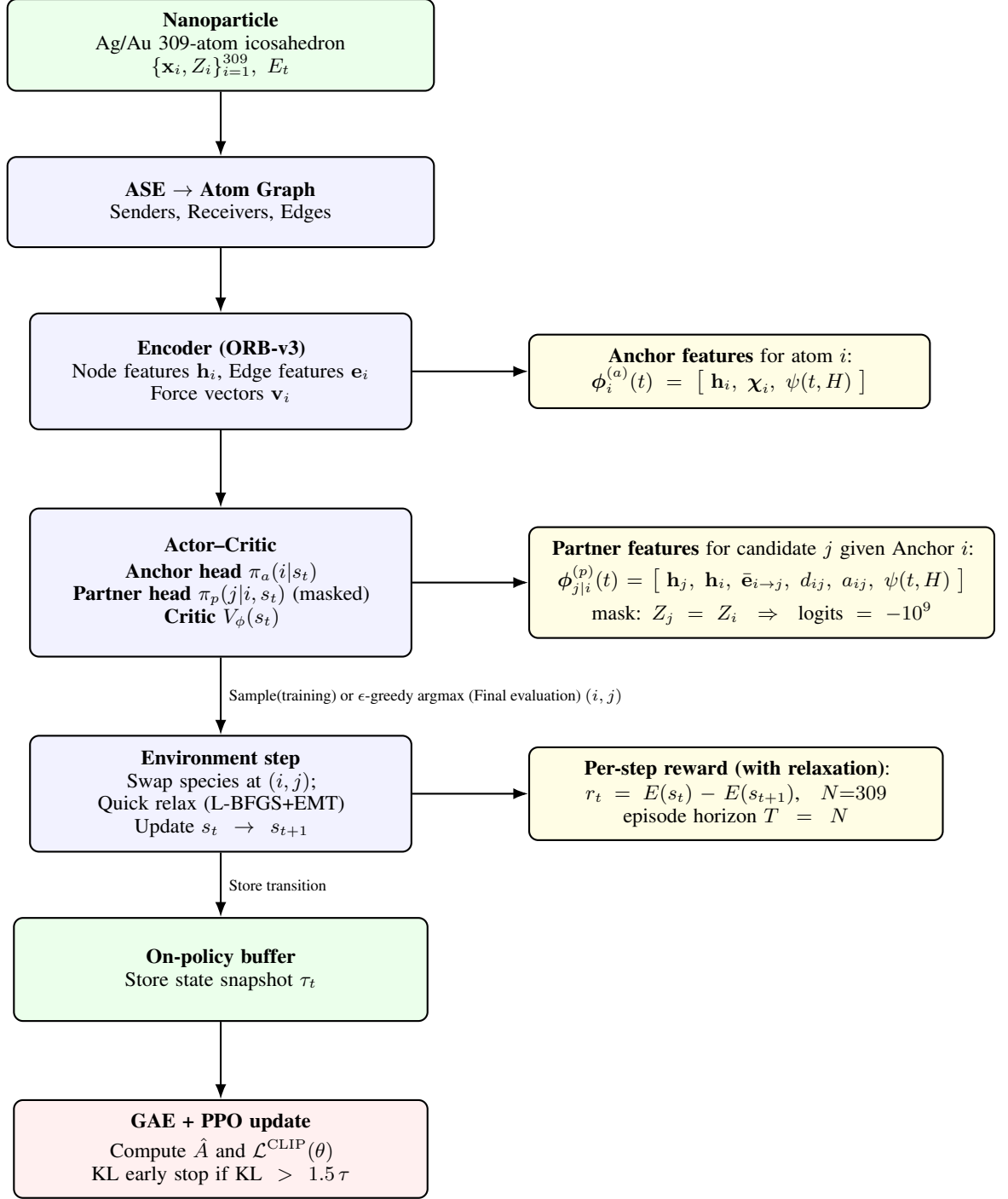
We use a factorised actor, which acts on features distilled from a frozen ORB-v3 atomic graph encoder (Rhodes et al., 2025). We use two neural network policy heads:

$$\pi_{\theta}(a_t | s_t) = \pi_{\theta_a}(i_t | s_t) \pi_{\theta_p}(j_t | s_t, i_t), \quad \theta = (\theta_a, \theta_p), \quad (1)$$

where θ_a are the features of the *anchor* policy neural network, and θ_p are the features of the *partner* policy neural network, which is conditioned on the chosen anchor atom indexed by i_t (See Appendix A.2 for details on how these policy networks are constructed).

3 Experimental Results and Discussion

Icosahedral NPs are used here to demonstrate the effectiveness of the proposed learning framework. Catalytic alloy NPs are often icosahedral, which are interesting due to the presence of a high density of edges/vertices, creating strained, low-coordination sites that can strongly modulate reaction intermediate adsorption energies. The discrete “magic-number” shells (N=13, 55, 147, 309, 561,...) also promote composition-dependent surface segregation and core–shell ordering, phenomena directly linked to catalytic selectivity and activity, and thus are critical to resolve accurately Ferrando et al. (2008). As a testbed for our model, icosahedra are ideal: they have clear, well-studied ground-state motifs, yet they have an enormous configuration space with many energetically near-degenerate arrangements Molayem et al. (2011a,b); Zhang & Fournier (2006). This creates a challenging test case, and effective policies must both discover the right shell assignments and avoid combinatorial traps. Their standardised sizes let us probe generalisation across composition with controlled geometry and later test size generalisation.



Validation compositions (Ag/Au, $N=309$):
 $8 \times \text{Ag}_X \text{Au}_{309-X}, X = \{296, 228, 205, 162, 126, 75, 25, 13\}$

Figure 2: PPO implementation and model flow for the proposed composition generalized model for global nanoparticle atomic ordering optimization.

Testing For final testing of the generalised agent, we treat the provably lowest energy structures with respect to the EMT potential established with MIP solutions of $\text{Ag}_X \text{Au}_{309-X}$ icosahedral nanoparticles

of Larsen et al. (2018) as reference targets, and use eight compositions whose ground state orderings were specifically reported there. At the end of training, each GPU samples a randomised configuration of these formulas, and the agent is tasked with solving these structures to find the minimum energy using an evaluation horizon $H_{eval} = 2 \times N_{atoms} = 618$.

In Figure 3, we show the single ordering (out of 8 - one for each GPU) found for each composition, which had the lowest final energy.

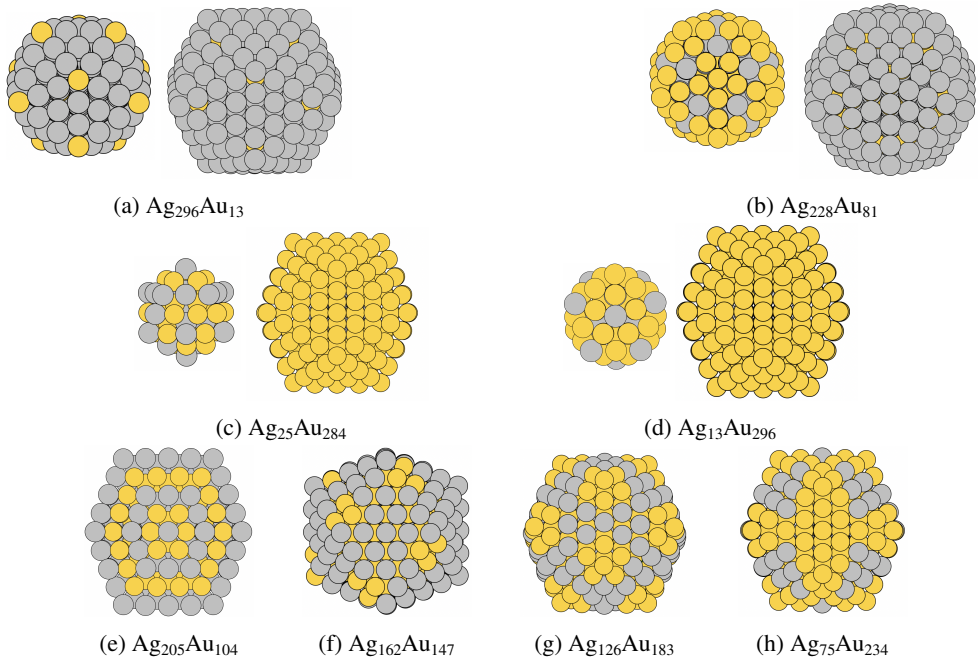


Figure 3: Lowest energy structures found by the trained agent for (a)-(h) the eight test compositions. For the first four (a)-(d) both the internal core structure (left) and outside shell structure (right) are provided.

3.1 Optimiser policy can generalise across composition (Experiment-1)

Current state-of-the-art models require running the ordering search individually from scratch for each elemental composition for an NP motif. A significant breakthrough can be achieved if a policy can be learnt that is general across compositions.

Training To evaluate composition generalisation of the model, we trained for 100 epochs \times 300 episodes on 309-atom icosahedra with fully randomised $\text{Ag}_X\text{Au}_{309-X}$ compositions and orderings (no ordering repeats). Training uses eight 24 GB RTX 3090 GPUs, each sampling distinct nanoparticles (varied by ordering and elemental composition) per episode. The horizon is $H_{train} = 309$, and for each step, the agent selects an anchor-partner pair, swaps them, relaxes the structure, and receives a reward $r_t = E(s_t) - E(s_{t+1})$. Because all states are similarly relaxed, r_t reflects only ordering improvements. We optimise actor-critic networks with PPO + GAE while keeping the ORB-v3 encoder frozen (Figure 2, see Appendix A for further details). We show training curves in Figure 6 in Appendix B.

Results For the structures dominated by a single species in Figures 3a-3d, we show both an interior view in the left figures and an exterior view of the shell in the right figures. For structures dominated by Ag (Figures 3a and 3b), the agent prefers an Ag-shell with Au atoms placed either at the subsurface corners (Figure 3a) or at the subsurface edges (Figure 3b). These structures are the same as the ground state structures found by Larsen et al. (2018). For structures dominated by Au (Figures 3c and 3d), the agent prefers an Au-shell with Ag atoms placed in the innermost 3 shells, with no Ag atoms in shells 4 and 5. The patterns of these structures are also similar to those found in Larsen et al. (2018), except for a few atoms. However, the agent correctly places an Ag atom in the centre

of these nanoparticles (in fact, all nanoparticles have a correctly placed central atom). For the more balanced compositions of Figures 3e-3h, the agent finds the same structures as those in Larsen et al. (2018), including the perfectly ordered "onion-shell" structure for $\text{Ag}_{205}\text{Au}_{104}$. The agent also finds the correct "flower-like" surface decoration of $\text{Ag}_{126}\text{Au}_{183}$ (Figure 3g), as well as the $\text{Ag}_{162}\text{Au}_{147}$ surface decoration with 3-atom clusters of Au (Figure 3f), and the $\text{Ag}_{75}\text{Au}_{234}$ surface decoration with 6-atom clusters of Ag (Figure 3h). These results affirm the suitability of our model towards generalisation across the chemical composition of a particular-sized icosahedral NP, lowering the cost of atomic ordering search through amortisation.

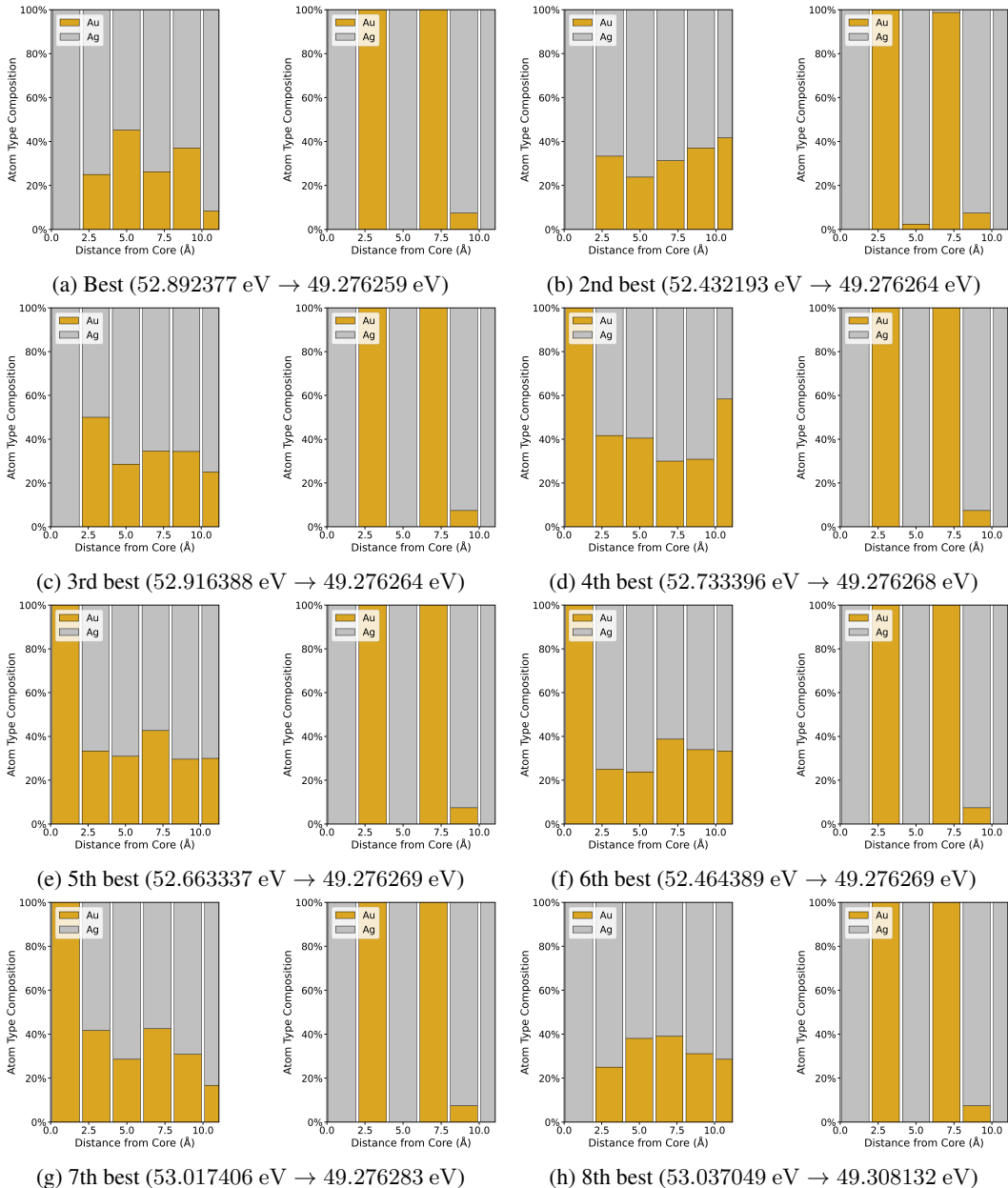


Figure 4: Elemental radial distribution function (E-RDF) plots and energies for eight initialised and final structures of icosahedral $\text{Ag}_{205}\text{Au}_{104}$. The panels (a)-(h) are ordered from lowest to highest.

To demonstrate the robustness of the policy-based optimisation of elemental ordering against random initialisation, we analyse eight final structures optimised by the agent from distinct random initialisations of the icosahedral $\text{Ag}_{205}\text{Au}_{104}$ (Figure 4). $\text{Ag}_{205}\text{Au}_{104}$ has a verifiably optimal "onion-shell"-like ground state ordering under the EMT potential (Larsen et al., 2018). This structure, which was

also found by the agent (see Figure 3e), has alternating layers of Ag and Au, starting with a central Ag atom, and thus has an easily recognisable signature in the elemental radial distribution function (E-RDF) plots. In Figure 4(a)-(h), we order the eight solutions found by the agent from different random initializations from the lowest final energy (best) (Figure Figure4(a), which is that of the configuration in Figure 3e) to the highest final energy (worst). The E-RDF for the randomised initial configurations (left) and for the agent’s final structure (right) show that in all cases the agent recovers the shell structure despite varied initialisations, and the energy gaps between (a) and the others are negligible ($\approx 10^{-5}$ meV/atom). The sole outlier (the worst structure, Figure4(h)) reflects sub-optimal relaxation, and the energy delta is ≈ 0.1 meV/atom to Figure4(a), yet the elemental ordering and E-RDF remain visually identical.

3.2 Policy generalisation allows extrapolation to different-sized NP (Experiment-2)

Extending the success of the model in generalising over alloy compositions, the next step towards achieving a universal alloy NP structure solver is size generalisation and extrapolation capabilities of the policy to unseen-sized NP motifs.

Training To test whether the agent’s policy can learn size-invariant ordering rules for icosahedral NP, we train on $\text{Ag}_x\text{Au}_{N-x}$ nanoparticles with $N \in \{55, 147, 561\}$ while *excluding* $N = 309$ NPs during the training process. We then evaluate the agent’s ability to resolve the lowest energy structure of 309-atom NPs. For consistency of comparison, we check the structures for the same eight Ag-Au compositions (ico-1 to ico-8 in Figure 5) as described in the previous section taken from Larsen et al. (2017).

Results Comparing the energies of 309 atom NPs (ico-1 to ico-8) optimised with the policy from experiment 1 (trained with 309 atom NPs) against the same NPs optimised with the policy from this experiment (never seen 309 atom NPs during training) provides a benchmark of the model’s capability in size extrapolation. Figure 5 shows that deploying the policy for unseen sized NP optimisation leads to a slight increase in the energy of the most stable structure found in some cases. The mean ΔE between the minimum energy structures from these two policies across systems is ≈ 0.021 eV (see table 1). The robustness of finding the lowest energy structure when optimising from different starting points is also preserved when extrapolating to 309 atom NP, similar to experiment 1. These results indicate that the learnt policy can be reliably transferred across icosahedral shell counts when the alloying elements are consistent.

System	E2 Δ Avg	E2 Δ Best	E2 Δ Worst	E3 Δ Avg	E3 Δ Best	E3 Δ Worst	Exp1 spread
ico-1	-0.010	0.000	-0.106	0.196	0.115	0.222	0.133
ico-2	-0.014	-0.000	-0.118	0.079	0.028	0.073	0.141
ico-3	0.014	0.000	0.015	0.053	0.033	0.065	0.032
ico-4	0.015	0.012	0.063	0.342	0.330	0.351	0.040
ico-5	0.103	0.095	0.101	0.412	0.355	0.468	0.053
ico-6	0.025	0.025	0.024	0.431	0.367	0.480	0.073
ico-7	0.026	0.005	0.077	0.148	0.074	0.230	0.016
ico-8	0.091	0.029	0.172	0.037	0.002	0.099	0.024
Mean	0.031	0.021	0.028	0.212	0.163	0.248	0.064

Table 1: For each of the eight test 309 atom alloy nanoparticles, the average, lowest and highest energy(eV) after optimisation in experiment 2 (E2) and experiment 3 (E3) is reported relative to the average, lowest and highest energy after optimisation in experiment 1. The maximum to minimum energy range (Exp1 spread) of the final state indicates intrinsic variability within multiple runs for a specific NP case (ico-1 to ico-8).

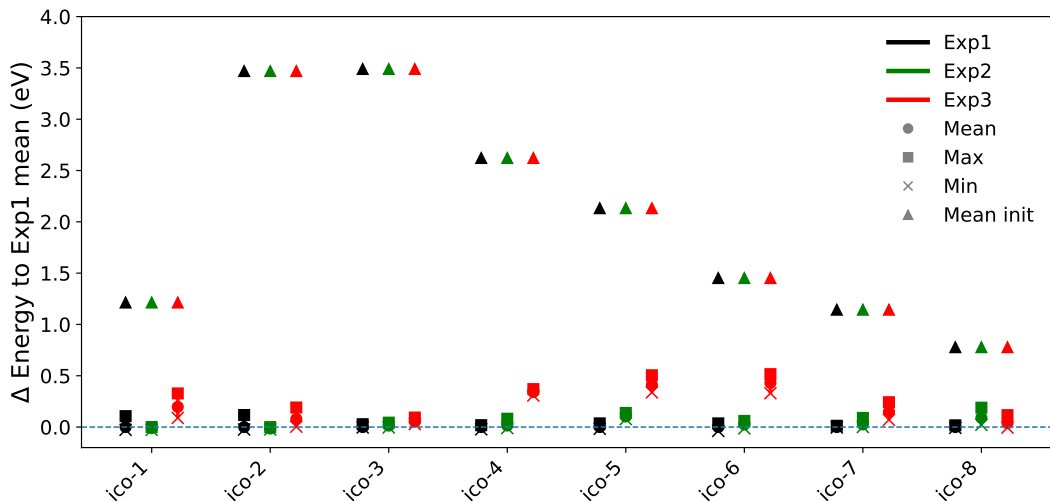


Figure 5: For all eight 309 atom test systems (ico-1 to ico-8), the summary of energies is shown as ΔE relative to the average energy of the final optimised structures from eight runs with policy from experiment 1 (dashed line). For each system, we depict the mean energy of the randomly initialised structure; the mean, maximum and minimum energies after optimisation of the structures from all runs. The dashed line at 0 denotes the baseline mean optimised structure energy from experiment 1. Optimisation runs from experiment 2 remain consistent and close to the results obtained in experiment 1. Experiment 3 results show that the policy trained with NPs of multiple element combinations fails to resolve the lowest energy structures in the size extrapolation situation. e.g. for ico-5 and ico-6 the the outcomes from different optimisation runs are consistently more than 0.3eV higher in energy than structures found in experiment 1.

3.3 Limited effectiveness in size extrapolation for cross-chemistry generalised policy (Experiment-3)

A model that can generalise among many different alloy elements and extrapolate to different sized NP can essentially be used to build foundational NP structures solvers that can be deployed across all elements and NP sizes.

Training To test the possibility of achieving multi-element generalisation and size extrapolation jointly, we added a second bimetallic chemistry during training and checked for robustness and transferability. We trained on both Ag–Au and Pt–Ni for NP sized $N \in \{55, 147, 561\}$, while excluding $N = 309$, and the policy was evaluated on the eight Ag–Au 309-atom NP as in the previous two experiments.

Results Introducing Pt–Ni and Ag–Au together in training makes the policy less reliable in finding the optimal structure of unseen 309-atom NPs. Energies of the final optimised structure proposed by this policy trend are noticeably higher than those of experiments 1 or 2 (Fig. 5). On average, the mean energy of optimised structures increases by ≈ 0.21 eV between systems, with the largest deviations observed for ico-5 and ico-6. Even considering the most stable optimised structure from each system, the optimised energy increases by ≈ 0.16 eV. Some systems remain less affected (e.g., ico-8), but the optimised NP energy is consistently worse than Exp1 and therefore overall is unreliable for optimisation of the NP structure. This points to a chemistry-induced distribution shift: mixing chemistries with distinct ordering energetics biases the policy away from Ag–Au motifs that were optimal in experiment 1.

4 Conclusion

In this work, we have shown that, utilising a molecular graph representation, an RL agent can reproduce provably optimal ground state nanoparticle orderings. The agent finds these orderings for varying compositions and can converge on identical optimal solutions from differently ordered

initialisations of the same chemical composition. The proposed architecture and training scheme allow for successful deployment of the agent for NPs that have a different size than training NPs, but this size extrapolation is not robust if multiple different element combinations must be tackled with the same policy.

In the future, this RL framework needs to be further developed to enable generalisation to larger combinatorial spaces, encompassing more atoms, atomic species, and other nanoparticle motifs and morphologies. The wider chemical space of NPs remains beyond the reach of traditional methods such as genetic algorithms and minimum integer programming. The search cost scales superlinearly while the objective landscape grows more complex. With RL, we hope to amortise exploration by learning transferable action priors and value estimates that can guide sampling toward high-yield regions with potentially fewer energy calls than naive search.

On the implementation side, the currently used frozen ORB-v3 backbone is a pragmatic choice, but its pretraining emphasises crystalline bulk datasets (e.g. MPtraj, Alexandria) rather than nanoparticles. Although the architecture supports non-periodic systems, nanoparticle or surface-specific data are missing in the training set. Future iterations of our agent could thus benefit from, e.g., nanoparticle-trained interatomic potentials and/or from performing end-to-end fine-tuning of the encoder jointly with the policy/value heads on NP data. A complementary direction is to replace expensive per-step relaxations with learnt relaxations. In Figure 3, we observed that in the final proposed structure from RL, a few atoms can be placed sub-optimally compared to the ideal solution. One reason for this could be that we currently have no mechanism to prevent energy-increasing moves late in the episode, because same-species swaps are explicitly prohibited by masking. In practice, the agent thus currently learns to keep swapping atoms back and forth between the same positions in an attempt to maintain an optimal structure. This is not ideal, so an improvement to our method could be to implement a mechanism to avoid forcing non-productive moves. Accordingly, we will experiment with the removal of the same-species mask and introduce either a no-operation/stop action or a variable-length horizon. The latter could be implemented by introducing a per-step penalty to discourage unnecessary swaps. Together, these changes might let the agent preserve the already optimal structures, anticipate relaxation effects, and generalise better as we expand our model to include more elements, nanoparticle sizes, and motifs.

5 Data availability statement

The codebase for this work will be openly available after peer review and formal acceptance.

6 Acknowledgments

We received funding from DNRF for the Pioneer Center for Accelerating P2X Materials Discovery (CAPEX) grant number P3, from the Det Frie Forskningsråd for Project “Data-driven quest for TWh scalable Na-ion battery (TeraBatt)” (2035-00232B) and “Autonomous agents of Discovery for earth-Abundant Na-ion battery cathodes (ADANA)” (3164-00297B). We also thank the Novo Nordisk Foundation Data Science Research Infrastructure 2022 Grant: A high-performance computing infrastructure for data-driven research on sustainable energy materials, Grant no. NNF22OC0078009.

A Algorithm details

Below, we detail the algorithm and implementation choices we have made. A graphical overview of the method is provided in Figure 2.

A.1 MDP and rewards

Each episode is a finite-horizon MDP

$$\mathcal{M} = (\mathcal{S}, \mathcal{A}, P, r, H, \gamma),$$

over a 309-atom icosahedral nanoparticle with a fixed random composition $\text{Ag}_x\text{Au}_{309-x}$ and randomly initialised ordering/positions. Here \mathcal{S} is the state space, \mathcal{A} the discrete action space, $P : \mathcal{S} \times \mathcal{A} \rightarrow \Delta(\mathcal{S})$ is the transition kernel $P(s'|s, a)$, $r : \mathcal{S} \times \mathcal{A} \times \mathcal{S} \rightarrow \mathbb{R}$ is the reward function, $H \in \mathbb{N}$ is the episode length, and $\gamma \in [0, 1]$ is the discount. In our environment, the transition $s_{t+1} \sim P(\cdot | s_t, a_t)$ is the *swap+relaxation* step (Fig. 1). In our setup, this transition is approximately deterministic. E_t is the potential energy after step t , and E_0 is the initial energy of the randomised configuration of the nanoparticle. With per-step relaxation we define the instantaneous reward

$$r_t = E_{t-1} - E_t, \quad t = 1, \dots, H, \quad (2)$$

Because we do not use a discount factor for our rewards, *i.e.* $\gamma = 1$, the telescoping property holds exactly for our setup:

$$G = \sum_{t=0}^{H-1} r_t = \sum_{t=0}^{H-1} (E_t - E_{t+1}) = E_0 - E_1 + E_1 - E_2 + \dots + E_{T-1} - E_T = E_0 - E_H, \quad (3)$$

so maximizing undiscounted return is equivalent to minimizing final energy. We interface with the nanoparticle using the Atomic Simulation Environment (ASE) (Larsen et al., 2017), and similarly compute energies in ASE.

For these calculations, we use the Effective Medium Theory (EMT) potential implemented in ASE (Jacobsen et al., 1987, 1996). EMT is a semi-empirical tight-binding/second-moment-type model in which the total energy decomposes into a short-ranged repulsive pair term plus an embedding contribution that depends on a locally accumulated electron density from neighbours. Both contributions are modeled by decaying exponentials with element-specific parameters fitted to reproduce bulk lattice constants, cohesive energies, bulk moduli and vacancy formation energies of the pure elements. Heteronuclear (alloy) interactions follow the standard EMT mixing rules implemented with the same parameter set. These parameters are fitted to reproduce experimental and Density Functional Theory (DFT) data for the elemental metals Ni, Cu, Ag, Au, Pd, Pt and bimetallic alloys (Jacobsen et al., 1996). EMT thus captures the correct trends in relative stabilities of different configurations, such as the energetic ordering of alloy structures or cluster isomers (Lysgaard et al., 2014). In practice we use the compiled ASAP implementation, which provides a vectorized neighbor-list kernel in C/C++ with OpenMP parallelism. Since we work with nanoparticles, we disable periodic boundary conditions and add 10 Å of vacuum so that EMT’s short cutoff does not couple periodic images. To perform local relaxations, we use the line-search L-BFGS optimizer (Liu & Nocedal, 1989) implemented in ASE. We use a maximum-force parameter f_{\max} to decide when to stop the relaxation, $\max_i \|\mathbf{F}_i\|_{\infty} \leq f_{\max}$ or alternatively when a step budget N_{\max} is reached. In practice we use small relaxations at intermediate steps ($f_{\max} = 0.01$, $N_{\max} = 1000$) and a stricter final relaxation at $t=H$ ($f_{\max} = 5 \times 10^{-3}$, $N_{\max} = 1000$). The reward is the energy drop after the *swap+relax* step has taken place.

A.2 State encoding and factorized policy

At time step t , the state s_t is the current nanoparticle (symbols and positions), which we encode using a pretrained ORB-v3 encoder (Rhodes et al., 2025). This yields per-atom embeddings $\mathbf{h}_i \in \mathbb{R}^{D_0}$ for atom i . The action is a swap $a_t = (i_t, j_t)$ between an *anchor* index i_t and a *partner* index j_t . We parameterize the joint policy by a factorization

$$\pi_{\theta}(a_t | s_t) = \pi_{\theta_a}(i_t | s_t) \pi_{\theta_p}(j_t | s_t, i_t), \quad (4)$$

with $\theta = (\theta_a, \theta_p)$.

Time embedding. We make the policy explicitly time-aware by concatenating a fixed, non-learned positional code of the current step and a scale indicator of the episode length. Let $t \in \{0, \dots, H-1\}$ denote the step index and H the horizon. We define

$$\psi(t, H) = [PE(t), \log H] \in \mathbb{R}^{d+1},$$

where $PE(t) \in \mathbb{R}^d$ is the sinusoidal code

$$PE_{2m}(t) = \sin\left(\frac{t}{10000^{2m/d}}\right), \quad PE_{2m+1}(t) = \cos\left(\frac{t}{10000^{2m/d}}\right), \quad m = 0, \dots, \frac{d}{2} - 1.$$

The inclusion of $\log H$ conditions the policy on the remaining budget. While we use fixed horizons due to the fixed particle size, we aim to use this to promote transfer across tasks with different horizons in future implementations where particle sizes and motifs vary. In implementation, $\psi(t, H)$ is tiled to all atoms so that each per-atom feature vector at time t carries identical temporal context. In theory, this design breaks step-exchange symmetry (action preferences near the end of an episode may differ from those early on).

Anchor head. Let $\mathbf{h}_i \in \mathbb{R}^{D_0}$ be the per-atom embedding from the pretrained ORB-v3 encoder for atom i . The ORB-v3 encoder also outputs an $\ell=1$ vector channel $\mathbf{v}_i \in \mathbb{R}^3$, which is a predicted force per atom. In our implementation, we recognize that the ORB-v3 model is not tailored to nanoparticles, and thus the predicted forces \mathbf{v}_i are not used directly to, e.g., relax the structure, but only used as force/dispersion "proxies", whose relation (if any) to the optimal ordering is learned inside the policy networks. To produce the anchor policy distribution, we compress this force proxy to a rotation-invariant scalar $\|\mathbf{v}_i\|_2$ and map it through a small MLP to obtain $\chi_i \in \mathbb{R}^{d_\chi}$. We provide χ_i to the agent in order to incentivize toward atoms with large local directional signal (high stress/instability), while $\|\mathbf{v}_i\|_2 = \|R\mathbf{v}_i\|_2$ for any $R \in \text{SO}(3)$ ensures frame-invariant logits. The time-aware anchor features are

$$\phi_i^{(a)}(t) = [\mathbf{h}_i, \chi_i, \psi(t, H)] \in \mathbb{R}^{D_0+d_\chi+(d+1)}. \quad (5)$$

An MLP $g_{\theta_a} : \mathbb{R}^{D_0+d_\chi+(d+1)} \rightarrow \mathbb{R}$ produces a scalar logit for each atom,

$$z_i^{(a)} = g_{\theta_a}(\phi_i^{(a)}(t)), \quad (6)$$

and the anchor distribution over indices $\{1, \dots, N\}$ is the categorical

$$\pi_{\theta_a}(i | s_t) = \text{softmax}(z^{(a)})_i \quad \text{with} \quad z^{(a)} = (z_1^{(a)}, \dots, z_N^{(a)}). \quad (7)$$

We do not rule out any atoms at the anchor stage (all atoms may serve as anchors). Instead, any masking is deferred to the partner head. Computationally, the anchor pass is $O(N)$ and $\psi(t, H)$ is broadcast to all atoms at step t .

Partner head (conditional on i). Given a sampled anchor i , we concatenate to each candidate partner atom indexed by j the embedding \mathbf{h}_j and the broadcast anchor embedding \mathbf{h}_i . We also augment the partner candidate features with two E(3)-invariant pairwise descriptors:

$$d_{ij} = \|x_j - x_i\|_2, \quad a_{ij} = \mathbf{v}_i^\top \mathbf{v}_j \quad (8)$$

where d_{ij} is a radial separation and a_{ij} is a force-alignment term derived from the encoder's force predictions. Similar to the anchor features, the relation to the force-alignment term is learned, and the forces are not used directly. These two terms thereby inject a lightweight physics prior, allowing the policy to learn a signed preference (favor or penalize) for near-field swaps conditioned on these descriptors, while keeping the logits frame-invariant. The full partner features are therefore

$$\phi_{j|i}^{(p)}(t) = [\mathbf{h}_j, \mathbf{h}_i, \bar{\mathbf{e}}_{i \rightarrow j}, d_{ij}, a_{ij}, \psi(t, H)], \quad (9)$$

passed through an MLP g_{θ_p} to produce logits $z_j^{(p,i)} = g_{\theta_p}(\phi_{j|i}^{(p)})$. Feasibility is enforced by a masked categorical

$$\pi_{\theta_p}(j | s_t, i) = \text{softmax}(z^{(p,i)} + \mathbf{m}_{s_t, i})_j, \quad \mathbf{m}_{s_t, i}(j) = \begin{cases} -\infty, & Z_j = Z_i, \\ 0, & \text{otherwise,} \end{cases} \quad (10)$$

which prohibits same-species swaps and (therefore) self-swaps, which has the added effect of reducing the effective action space while preserving correct invariances of the logits.

Critic and value pooling. The value function $V_\phi(s_t)$ shares the time-aware per-atom inputs with the anchor head. We compute two permutation-invariant summaries of the per-atom features $\{h_i(t)\}_{i=1}^N$: a feature-wise attention pool $p^{(1)}$ and a uniform mean $p^{(2)}$. Let $a(h_i) \in \mathbb{R}^D$ be the output of a learned scoring MLP applied to h_i . For each feature channel d ,

$$W_{i,d} = \frac{\exp(a_d(h_i))}{\sum_{k=1}^N \exp(a_d(h_k))}, \quad p_d^{(1)} = \sum_{i=1}^N W_{i,d} h_{i,d}, \quad (11)$$

and

$$p^{(2)} = \frac{1}{N} \sum_{i=1}^N h_i. \quad (12)$$

Two MLP heads produce scalars $v_1 = v_{\phi_1}(p^{(1)})$ and $v_2 = v_{\phi_2}(p^{(2)})$. The final value is a gated sum

$$V_\phi(s_t) = \sigma(w_1) v_1 + \sigma(w_2) v_2, \quad \phi = (\phi_1, \phi_2)$$

where $w_1, w_2 \in \mathbb{R}$ are learnable scalars updated by backprop through the value loss and $\sigma(\cdot)$ is the logistic sigmoid. This dual value network strategy is inspired by twin-critic architectures (Hasselt, 2010; Van Hasselt et al., 2016) in which two value estimators are trained in parallel. Their outputs are combined via a learnable weighted sum, providing lower bias and improved stability compared to a single critic. This is conceptually related to Double Q-learning and Clipped Double Q-learning, but differs in that we learn the aggregation weights rather than fixing them.

A.3 GAE and bootstrapping

We collect trajectories until a target number of complete episodes is reached. Let $d_t \in \{0, 1\}$ be the terminal flag ($d_t=1$ if s_{t+1} is terminal). Define TD residuals

$$\delta_t = r_t + \gamma(1 - d_t) V_\phi(s_{t+1}) - V_\phi(s_t), \quad (13)$$

and generalized advantages (GAE) (Schulman et al., 2015b) with parameter $\lambda \in [0, 1]$, truncated at episode ends,

$$\hat{A}_t = \sum_{\ell \geq 0} (\gamma \lambda)^\ell \left(\prod_{m=0}^{\ell-1} (1 - d_{t+m}) \right) \delta_{t+\ell}, \quad \hat{R}_t = \hat{A}_t + V_\phi(s_t). \quad (14)$$

Equivalently, the backward recursion $\hat{A}_t = \delta_t + \gamma \lambda (1 - d_t) \hat{A}_{t+1}$ with $\hat{A}_T = 0$. We normalize $\{\hat{A}_t\}$ per episode.

At each step t we append a record $\tau_t = (A_t, i_t, j_t, r_t, d_t, t, H, \log \pi_{\text{old}}^{(a)}(i_t | s_t), \log \pi_{\text{old}}^{(p)}(j_t | s_t, i_t), V_{\phi, \text{old}}(s_t))$, where S_t is the state before the swap, (i_t, j_t) is the sampled (anchor, partner), r_t the reward, $d_t \in \{0, 1\}$ the terminal flag, (t, H) reconstruct the time code, $\log \pi_{\text{old}}^{(a)}, \log \pi_{\text{old}}^{(p)}$ are the detached headwise log-probs under the behavior policy, and $V_{\phi, \text{old}}(s_t)$ the detached critic value. We also cache the joint old log-prob $\log \pi_{\text{old}} = \log \pi_{\text{old}}^{(a)} + \log \pi_{\text{old}}^{(p)}$. After collecting a target number of complete episodes, we compute (\hat{A}_t, \hat{R}_t) and, during PPO updates, re-encode each stored \hat{A}_t with the current networks to obtain current logits/entropies, rebuild the same mask from atomic numbers, reconstruct $\psi(t, H)$ from (t, H) , and form the current joint log-prob $\log \pi_\theta = \log \pi_\theta^{(a)} + \log \pi_\theta^{(p)}$ used in the importance ratio and KL gate.

A.4 PPO objectives and loss

Given the factorized policy of Eq. (4), the joint log-probability used for training is

$$\log \pi_\theta(a_t | s_t) = \underbrace{\log \text{softmax}(\pi_{\theta_a}(i | s_t))}_{\text{anchor}} + \underbrace{\log \text{softmax}(\pi_{\theta_p}(j | s_t, i))}_{\text{partner}}. \quad (15)$$

Using the joint log-probability is necessary because the sampled action $a_t = (i_t, j_t)$ comes from a product distribution with a conditional partner head; equivalently,

$$\frac{\pi_\theta(a_t | s_t)}{\pi_{\theta, \text{old}}(a_t | s_t)} = \frac{\pi_{\theta_a}(i_t | s_t)}{\pi_{\theta_a, \text{old}}(i_t | s_t)} \cdot \frac{\pi_{\theta_p}(j_t | s_t, i_t)}{\pi_{\theta_p, \text{old}}(j_t | s_t, i_t)}. \quad (16)$$

With this, we define the importance ratio

$$\rho_t(\theta) = \frac{\pi_\theta(a_t | s_t)}{\pi_{\theta_{\text{old}}}(a_t | s_t)} = \exp \left(\log \pi_\theta(a_t | s_t) - \log \pi_{\theta_{\text{old}}}(a_t | s_t) \right). \quad (17)$$

Following PPO (Schulman et al., 2017), we optimize the clipped surrogate

$$\mathcal{L}^{\text{CLIP}}(\theta) = \mathbb{E}_t \left[\min \left(\rho_t(\theta) \hat{A}_t, \text{clip}(\rho_t(\theta), 1 - \epsilon, 1 + \epsilon) \hat{A}_t \right) \right], \quad (18)$$

where $\epsilon > 0$ is the trust-region width and \hat{A}_t is the (per-episode normalized) generalized advantage estimate (Schulman et al., 2015b). Here we have taken an ϵ -greedy strategy ($\epsilon = 0.05$). The clipping term is an unconstrained proxy for the trust-region penalty (Schulman et al., 2015a), limiting harmful updates when ρ_t deviates too far from 1 with $\hat{A}_t \neq 0$. We then combine the policy surrogate with a value regression and entropy regularization and minimize

$$\mathcal{J}(\theta, \phi) = -\alpha_{\text{pol}} \mathcal{L}^{\text{CLIP}}(\theta) + \alpha_{\text{vf}} \mathbb{E}_t \left[\ell_{\text{SmoothL1}}(V_\phi(s_t), \hat{R}_t) \right] - \alpha_{\text{ent}} \mathbb{E}_t \left[H(\pi_{\theta_a}(\cdot | s_t)) + H(\pi_{\theta_p}(\cdot | s_t, i_t)) \right], \quad (19)$$

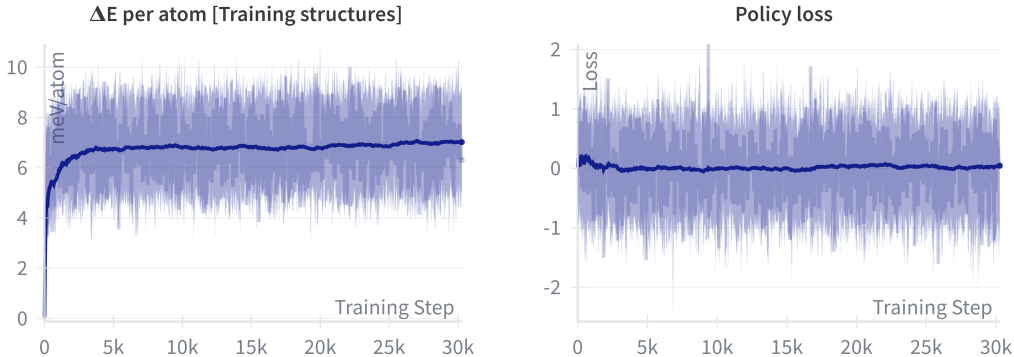
with coefficients $\alpha_{\text{pol}}, \alpha_{\text{vf}}, \alpha_{\text{ent}} > 0$. Here $\hat{R}_t = \hat{A}_t + V_\phi(s_t)$ is the bootstrap target and ℓ_{SmoothL1} is the Huber loss (Huber, 1992), chosen for robustness to occasional large post-relaxation energy drops (heavy-tailed targets). Entropies $H(\cdot)$ are computed on the masked categoricals and encourage exploration in both heads (Williams, 1992; Mnih et al., 2016).

KL gating (early stopping). To further bound policy drift across PPO epochs, we monitor the empirical *joint* KL on each mini-batch,

$$\widehat{\text{KL}}(\pi_{\text{old}} \| \pi_\theta) = \mathbb{E}_t \left[\log \pi_{\text{old}}(a_t | s_t) - \log \pi_\theta(a_t | s_t) \right], \quad (20)$$

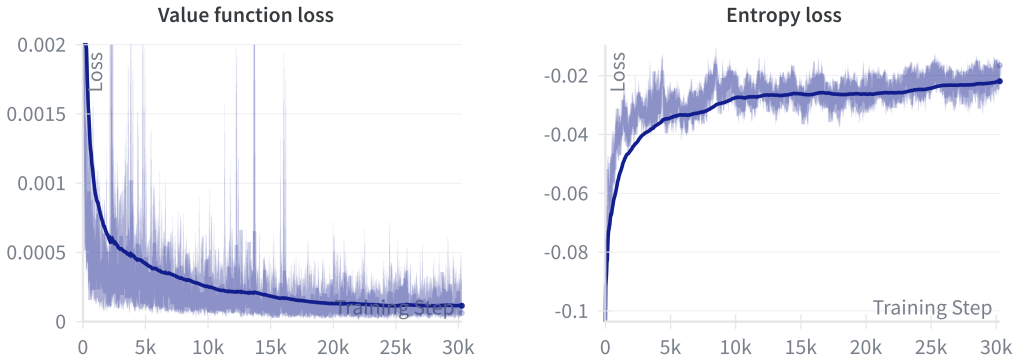
computed with Eq. (15) over the masked feasible set. If $\widehat{\text{KL}} > c_{\text{stop}} \cdot \tau$ with $c_{\text{stop}} = 1.5$ and τ being a target max KL divergence (a hyperparameter set to 0.015 in our experiments), we stop the current PPO epoch early (break the mini-batch loop). This empirically prevents collapse and aligns with the trust-region motivation of TRPO/PPO (Schulman et al., 2015a, 2017).

B Training curves



(a) Training progress for the energy reduction per atom over the full training horizon, in meV/atom

(b) Training progress for the policy loss



(c) Training progress for the value function loss

(d) Training progress for the entropy loss

Figure 6: Training curves for our RL agent. **(a)**: The pattern is typical for a well-posed PPO procedure, with return rising over time. In this case, we display the final energy reduction per atom, which is proportional to the return G , i.e. $\frac{\Delta E}{atom} = \frac{E_0 - E_H}{N_{atoms}} = \frac{G}{N_{atoms}}$ (see Equation 3). **(b)**: Since we use advantage normalization (GAE), the expectation value of the advantage \hat{A} is $\mathbb{E}[\hat{A}] \approx 0$, and near a local optimum the importance ratio (Equation 17) is $\rho_t \approx 1$, so the expected surrogate is near zero. Furthermore, clipping plus KL gating keeps ρ_t close to 1, which further dampens any trend. Finite-sample noise, changing data (on-policy), and alternating updates of policy/critic then produce batches where \mathcal{L}^{CLIP} is slightly positive or negative. Thus, the observed oscillation around 0 is expected. **(c)**: Meanwhile, the value loss falls because V_ϕ learns to match the bootstrap targets, shrinking TD errors over time. **(d)**: As the policy sharpens, the entropy $H(\pi)$ decreases as the policy more exploitative.

C Additional results

C.1 Full trajectory example

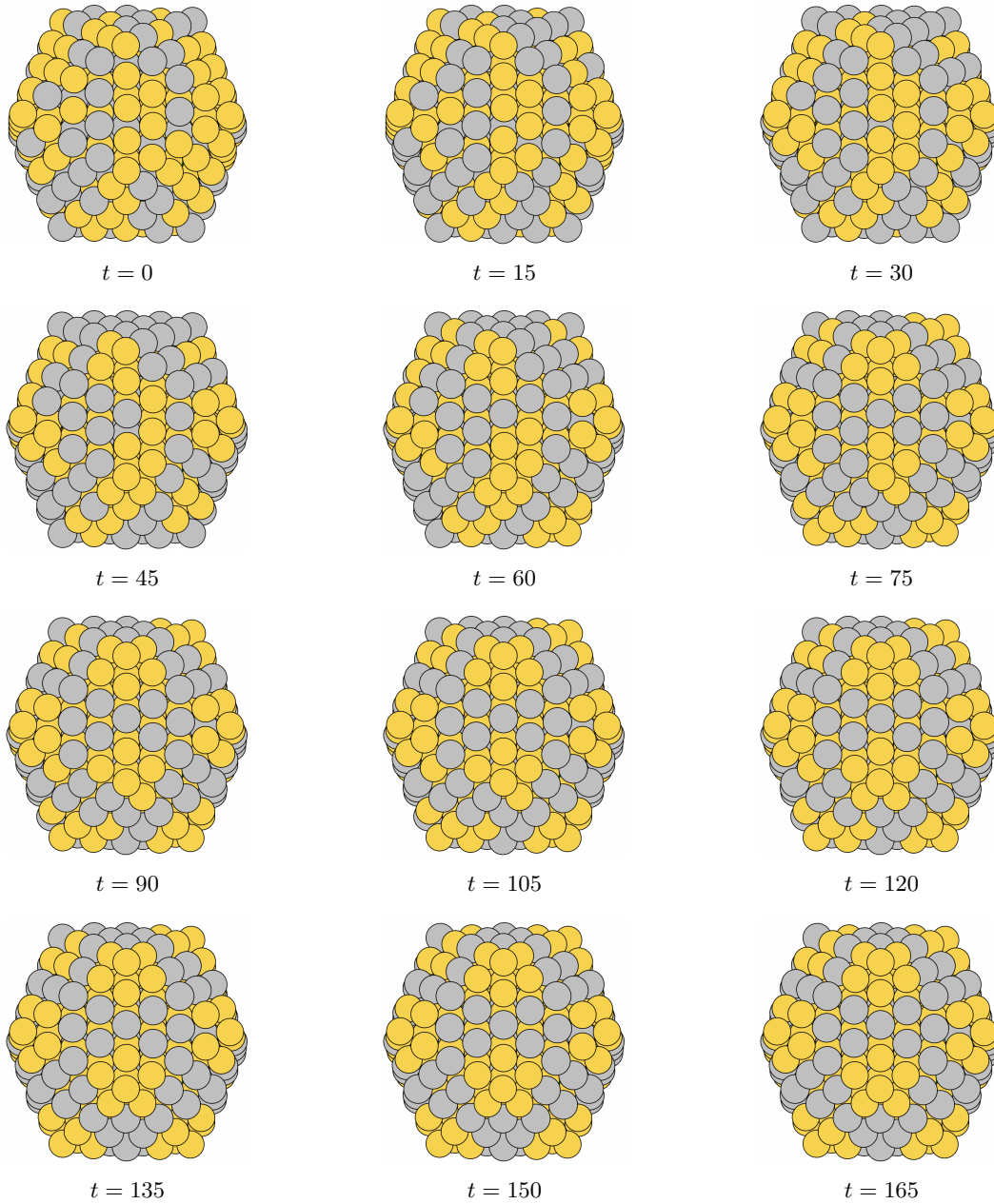


Figure 7: Snapshots from the first 165 steps (atomic swaps) for the best $\text{Ag}_{126}\text{Au}_{183}$ configuration found by the RL agent, which is equivalent to the provably optimal ordering found in (Larsen et al., 2018). As seen in the trajectory, most of the atoms in the final solution of Figure 3g are already in their final position at $t = 165$, even though the evaluation horizon is $H = 2 \times N_{atoms} = 618$. In particular, the top-left Ag atom is still out of place at $t = 165$ compared to Figure 3g, but the agent swaps this atom for Au around $t = 300$.

References

- Ahmed, N., Farooq, M. U., and Chen, F. Materials discovery through reinforcement learning: a comprehensive review. *AI & Materials*, 1(2):1–2, 2025.
- Álvarez-Zapatero, P., Vega, A., and Aguado, A. A neural network potential for searching the atomic structures of pure and mixed nanoparticles. application to znmg nanoalloys with an eye on their anticorrosive properties. *Acta Materialia*, 220:117341, 2021.
- Artrith, N. and Kolpak, A. M. Grand canonical molecular dynamics simulations of cu–au nanoalloys in thermal equilibrium using reactive ann potentials. *Computational Materials Science*, 110:20–28, 2015.
- Bochicchio, D. and Ferrando, R. Morphological instability of core-shell metallic nanoparticles. *Physical Review B—Condensed Matter and Materials Physics*, 87(16):165435, 2013.
- Bochicchio, D., Ferrando, R., Novakovic, R., Panizon, E., and Rossi, G. Chemical ordering in magic-size ag–pd nanoparticles. *Physical Chemistry Chemical Physics*, 16(48):26478–26484, 2014.
- Cerbelaud, M., Ferrando, R., Barcaro, G., and Fortunelli, A. Optimization of chemical ordering in agau nanoalloys. *Physical Chemistry Chemical Physics*, 13(21):10232–10240, 2011.
- Chen, F. and Johnston, R. L. Energetic, electronic, and thermal effects on structural properties of ag–au nanoalloys. *ACS nano*, 2(1):165–175, 2008.
- Cheng, D., Yuan, S., and Ferrando, R. Structure, chemical ordering and thermal stability of pt–ni alloy nanoclusters. *Journal of Physics: Condensed Matter*, 25(35):355008, 2013.
- Dean, J., Cowan, M. J., Estes, J., Ramadan, M., and Mpourmpakis, G. Rapid prediction of bimetallic mixing behavior at the nanoscale. *ACS nano*, 14(7):8171–8180, 2020.
- Elsborg, J. and Bhowmik, A. Equivariant graph-representation-based actor–critic reinforcement learning for nanoparticle design. *Journal of Chemical Information and Modeling*, 63(12):3731–3741, 2023.
- Elsborg, J. and Bhowmik, A. Artisan: navigating the complexity of material structures with deep reinforcement learning. *Machine Learning: Science and Technology*, 5(3):035043, 2024.
- Ferrando, R., Jellinek, J., and Johnston, R. L. Nanoalloys: from theory to applications of alloy clusters and nanoparticles. *Chemical reviews*, 108(3):845–910, 2008.
- Flam-Shepherd, D., Zhigalin, A., and Aspuru-Guzik, A. Scalable fragment-based 3d molecular design with reinforcement learning. *arXiv preprint arXiv:2202.00658*, 2022.
- Froemming, N. S. and Henkelman, G. Optimizing core-shell nanoparticle catalysts with a genetic algorithm. *The Journal of chemical physics*, 131(23), 2009.
- Gould, A., Heard, C., Logsdail, A., and Catlow, C. Segregation effects on the properties of (auag)₁₄₇. *Physical Chemistry Chemical Physics*, 16(39):21049–21061, 2014.
- Han, S., Barcaro, G., Fortunelli, A., Lysgaard, S., Vegge, T., and Hansen, H. A. Unfolding the structural stability of nanoalloys via symmetry-constrained genetic algorithm and neural network potential. *npj Computational Materials*, 8(1):121, 2022.
- Hasselt, H. Double q-learning. *Advances in neural information processing systems*, 23, 2010.
- Huber, P. J. Robust estimation of a location parameter. In *Breakthroughs in statistics: Methodology and distribution*, pp. 492–518. Springer, 1992.
- Jacobsen, K. W., Norskov, J., and Puska, M. J. Interatomic interactions in the effective-medium theory. *Physical Review B*, 35(14):7423, 1987.
- Jacobsen, K. W., Stoltze, P., and Nørskov, J. A semi-empirical effective medium theory for metals and alloys. *Surface Science*, 366(2):394–402, 1996.

- Larsen, A. H., Mortensen, J. J., Blomqvist, J., Castelli, I. E., Christensen, R., Duřak, M., Friis, J., Groves, M. N., Hammer, B., Hargus, C., et al. The atomic simulation environment—a python library for working with atoms. *Journal of Physics: Condensed Matter*, 29(27):273002, 2017.
- Larsen, P. M., Jacobsen, K. W., and Schiřtz, J. Rich ground-state chemical ordering in nanoparticles: Exact solution of a model for ag–au clusters. *Physical Review Letters*, 120(25):256101, 2018.
- Liu, D. C. and Nocedal, J. On the limited memory bfgs method for large scale optimization. *Mathematical programming*, 45(1):503–528, 1989.
- Liu, T.-D., Xu, L.-Y., Shao, G.-F., Tu, N.-N., Tao, J.-P., and Wen, Y.-H. Structural optimization of pt–pd–rh trimetallic nanoparticles using improved genetic algorithm. *Journal of Alloys and Compounds*, 663:466–473, 2016.
- Loevlie, D. J., Ferreira, B., and Mpourmpakis, G. Demystifying the chemical ordering of multimetallic nanoparticles. *Accounts of Chemical Research*, 56(3):248–257, 2023.
- Lysgaard, S., Landis, D. D., Bligaard, T., and Vegge, T. Genetic algorithm procreation operators for alloy nanoparticle catalysts. *Topics in Catalysis*, 57:33–39, 2014.
- Lysgaard, S., Mřrdal, J. S., Hansen, H. A., and Vegge, T. A dft-based genetic algorithm search for aucu nanoalloy electrocatalysts for co 2 reduction. *Physical Chemistry Chemical Physics*, 17(42):28270–28276, 2015.
- McIntyre, S. M. and Garden, A. L. Computational modelling of nanoparticle catalysis. *Nanoscale*, 17(24):14491–14520, 2025.
- Mnih, V., Badia, A. P., Mirza, M., Graves, A., Lillicrap, T., Harley, T., Silver, D., and Kavukcuoglu, K. Asynchronous methods for deep reinforcement learning. In *International conference on machine learning*, pp. 1928–1937. PmLR, 2016.
- Molayem, M., Grigoryan, V. G., and Springborg, M. Global minimum structures and magic clusters of cu m ag n nanoalloys. *The Journal of Physical Chemistry C*, 115(45):22148–22162, 2011a.
- Molayem, M., Grigoryan, V. G., and Springborg, M. Theoretical determination of the most stable structures of ni m ag n bimetallic nanoalloys. *The Journal of Physical Chemistry C*, 115(15):7179–7192, 2011b.
- Narayan, N., Meiyazhagan, A., and Vajtai, R. Metal nanoparticles as green catalysts. *Materials*, 12(21):3602, 2019.
- Negreiros, F. R., Kuntová, Z., Barcaro, G., Rossi, G., Ferrando, R., and Fortunelli, A. Structures of gas-phase ag–pd nanoclusters: a computational study. *The Journal of chemical physics*, 132(23), 2010.
- Ojha, A., Bulusu, S. S., Banerjee, A., et al. Ann and dft investigation of 55-atom icosahedral ag-pt nanoalloys: Understanding structure, dynamics, and o2 activation. *Computational and Theoretical Chemistry*, 1238:114691, 2024.
- Pirart, J., Front, A., Rapetti, D., Andrezza-Vignolle, C., Andrezza, P., Mottet, C., and Ferrando, R. Reversed size-dependent stabilization of ordered nanophases. *Nature Communications*, 10(1):1982, 2019.
- Rapallo, A., Rossi, G., Ferrando, R., Fortunelli, A., Curley, B. C., Lloyd, L. D., Tarbuck, G. M., and Johnston, R. L. Global optimization of bimetallic cluster structures. i. size-mismatched ag–cu, ag–ni, and au–cu systems. *The Journal of chemical physics*, 122(19), 2005.
- Rhodes, B., Vandenhaute, S., řimkus, V., Gin, J., Godwin, J., Duignan, T., and Neumann, M. Orb-v3: atomistic simulation at scale, 2025. URL <https://arxiv.org/abs/2504.06231>.
- Rodrigues, D. D., Nascimento, A. M., Duarte, H. A., and Belchior, J. C. Global optimization analysis of cunaum (n+ m= 38) clusters: Complementary ab initio calculations. *Chemical Physics*, 349(1-3):91–97, 2008.

- Rondina, G. G. and Da Silva, J. L. Revised basin-hopping monte carlo algorithm for structure optimization of clusters and nanoparticles. *Journal of chemical information and modeling*, 53(9): 2282–2298, 2013.
- Schulman, J., Levine, S., Abbeel, P., Jordan, M., and Moritz, P. Trust region policy optimization. In *International conference on machine learning*, pp. 1889–1897. PMLR, 2015a.
- Schulman, J., Moritz, P., Levine, S., Jordan, M., and Abbeel, P. High-dimensional continuous control using generalized advantage estimation. *arXiv preprint arXiv:1506.02438*, 2015b.
- Schulman, J., Wolski, F., Dhariwal, P., Radford, A., and Klimov, O. Proximal policy optimization algorithms. *arXiv preprint arXiv:1707.06347*, 2017.
- Simm, G., Pinsler, R., and Hernández-Lobato, J. M. Reinforcement learning for molecular design guided by quantum mechanics. In *International Conference on Machine Learning*, pp. 8959–8969. PMLR, 2020.
- Tao, J.-p., Ji, Q.-s., Shao, G.-f., Li, Z.-p., Liu, T.-d., and Wen, Y.-h. Stable structure optimization of pt-x-cu (x= au, ag, pd and rh) trimetallic nanoparticles. *Journal of alloys and compounds*, 716: 240–250, 2017.
- Van Hasselt, H., Guez, A., and Silver, D. Deep reinforcement learning with double q-learning. In *Proceedings of the AAAI conference on artificial intelligence*, volume 30,1, 2016.
- Williams, R. J. Simple statistical gradient-following algorithms for connectionist reinforcement learning. *Machine learning*, 8(3):229–256, 1992.
- Zhang, M. and Fournier, R. Structure of 55-atom bimetallic clusters. *Journal of Molecular Structure: THEOCHEM*, 762(1-3):49–56, 2006.
- Zhang, N., Chen, F., and Wu, X. Global optimization and oxygen dissociation on polyicosahedral ag₃₂cu₆ core-shell cluster for alkaline fuel cells. *Scientific reports*, 5(1):11984, 2015.